Commun Nonlinear Sci Numer Simulat 80 (2019) 104979

Contents lists available at ScienceDirect

Commun Nonlinear Sci Numer Simulat

journal homepage: www.elsevier.com/locate/cnsns

Research paper

Pseudo-plateau bursting and mixed-mode oscillations in a model of developing inner hair cells

Harun Baldemir[a,d], Daniele Avitabile[e,f], Krasimira Tsaneva-Atanasova[a,b,c,*]

[a] Department of Mathematics, University of Exeter, Exeter, EX4 4QF, UK
[b] Living Systems Institute, University of Exeter, Exeter, EX4 4QD, UK
[c] EPSRC Centre for Predictive Modelling in Healthcare, University of Exeter, Exeter, EX4 4QJ, UK
[d] Department of Mathematics, Cankiri Karatekin University, Cankiri, 18100, Turkey
[e] VU University Amsterdam, Department of Mathematics Faculteit der Exacte Wetenschappen De Boelelaan 1081a 1081 HV Amsterdam, The Netherlands
[f] Inria Sophia Antipolis Méditerranée Research Centre, MathNeuro Team, 2004 route des Lucioles-Boîte Postale 93 06902 Sophia Antipolis, Cedex, France

ARTICLE INFO

Article history:
Available online 23 August 2019

Keywords:
Excitable cells
Model reduction
Fast-slow analysis
Pseudo-plateau bursting
Mixed-mode oscillations

ABSTRACT

Inner hair cells (IHCs) are excitable sensory cells in the inner ear that encode acoustic information. Before the onset of hearing IHCs fire calcium-based action potentials that trigger transmitter release onto developing spiral ganglion neurones. There is accumulating experimental evidence that these spontaneous firing patterns are associated with maturation of the IHC synapses and hence involved in the development of hearing. The dynamics organising the IHCs' electrical activity are therefore of interest.

Building on our previous modelling work we propose a three-dimensional, reduced IHC model and carry out non-dimensionalisation. We show that there is a significant range of parameter values for which the dynamics of the reduced (three-dimensional) model map well onto the dynamics observed in the original biophysical (four-dimensional) IHC model. By estimating the typical time scales of the variables in the reduced IHC model we demonstrate that this model could be characterised by two fast and one slow or one fast and two slow variables depending on biophysically relevant parameters that control the dynamics. Specifically, we investigate how changes in the conductance of the voltage-gated calcium channels as well as the parameter corresponding to the fraction of free cytosolic calcium concentration in the model affect the oscillatory model bahaviour leading to transition from pseudo-plateau bursting to mixed-mode oscillations. Hence, using fast-slow analysis we are able to further our understanding of this model and reveal a path in the parameter space connecting pseudo-plateau bursting and mixed-mode oscillations by varying a single parameter in the model.

* Corresponding author at: Living Systems Institute, University of Exeter, Exeter, EX4 4QD, UK.
E-mail address: k.tsaneva-atanasova@exeter.ac.uk (K. Tsaneva-Atanasova).

https://doi.org/10.1016/j.cnsns.2019.104979

1. Introduction

Inner hair cells (IHCs) are responsible for sound transduction as 90–95% of the afferent fibres of the auditory nerve connect to IHCs via synapses. As many other physiological systems, these synapses undergo a process of maturation during development of hearing [1,2]. There is a growing body of experimental evidence suggesting that this maturation involves spontaneous, calcium-dependent electrical activity in the form of complex action potentials [2–5]. Specifically, the calcium (Ca^{2+}) signals associated with the spontaneous electrical activity observed in immature IHCs trigger neurotransmitter release, which generates action potentials in auditory neurones [6,7]. The action-potential firing in auditory neurones is thought to be important for the development of the auditory system in terms of tonotopic (or frequency specific) organisation [8].

The electrical activity typically observed in immature IHCs is a combination of classical action potentials [9,10] and prolonged action potentials that feature small plateau oscillations, called *pseudo-plateau bursting* [11–15]. These action potentials are accompanied by Ca^{2+} signals that in turn modulate their amplitude and duration [16,17]. As mentioned above, the significance of the Ca^{2+} dynamics observed in immature IHCs lies in its importance for neurotransmitter release and signalling downstream the auditory pathway [6,7]. Specifically, prolonged action potentials generate Ca^{2+} signals characterised by larger amplitude and longer duration compared to normal action potentials [17] and correspond to a greater amount of calcium entry, which in turn could result in a larger amount of neurotransmitter release [7,18].

In earlier work [16,17] we have proposed a biophysical model of immature IHCs that generates oscillations of the membrane potential in the form of single spikes, plateau-bursting and a mixture of spikes and bursts. This model has been parametrised using available experimental data obtained by recording the main ion-channel currents found in immature IHCs [1,5,19–22]. Interestingly such complex oscillatory behaviour have been also reported recently in a reduced model of the *Xenopus* tadpole central pattern generator, which is also a developmental system (see Figure 9B in [23]). Our model is of Chay and Keizer type [10] and represents a modification of the Hodgkin–Huxley model equations [9] including Ca^{2+} currents coupled to an additional equation describing the dynamics of the intracellular calcium concentration ($[Ca^{2+}]_i$). There are several biophysical parameters in the model that directly control the dynamics of calcium including the maximal K_{Ca} channels conductance, $g_{K_{Ca}}$, and the ER leak rate, p_{ER}. The role of $g_{K_{Ca}}$ and p_{ER} in shaping the patterns of electrical activity in IHCs has been previously analysed and compared to experimental observations, keeping all other model parameters at a fixed, biophysically plausible values [16,17].

This article advances our understanding of the mechanisms controlling IHCs electrical activity and intracellular Ca^{2+} dynamics by investigating the effect of varying the maximal Ca^{2+} channel conductance, g_{Ca}. We show that changes in g_{Ca} have a dramatic effect not only on the model solutions, but also on the characteristic time scale constants of the model. This is important because the maximal Ca^{2+} channel conductance is proportional to the number of Ca^{2+} channels, which most likely also varies during development of hearing [24] and are essential in IHCs [25]. Another significant contribution of this study is the derivation of a reduced (3-dimensional) version of the immature IHC's model that facilitates the application of fast-slow analysis and allows us to understand better the solutions originally observed in the full (4-dimensional) model. Specifically, using the reduced IHC model we are able to systematically investigate the complex oscillations observed in IHCs in the full 3-dimensional phase space.

We start by demonstrating in Section 2 that the number of large (normal) spikes of complex periodic orbits decreases and, eventually, complex solutions become pseudo-plateau bursting solutions as g_{Ca} increases. To do so, we perform numerical bifurcation analysis of both the original 4-dimensional as well as reduced 3-dimensional IHC models applying an approach similar to that taken in [17]. Thus, we are able to show that the reduced IHC model can generate similar dynamics as the original IHC model using the same set of parameter values. Importnatly, non-dimensionalisation of the model provides the characteristic time-scale constants that indicate the relative rates of change of the state variables. We use this information to classify the model variables into fast and slow.

In Section 3, we perform a fast-slow analysis [26] of the reduced IHC model. We show that this model could be characterised by two fast and one slow or one fast and two slow variables, depending on the choices of the parameters. Therefore, as we change model parameters, we switch the technique used to interpret activity patterns, from *2-fast/1-slow analysis* [27] to *1-fast/2-slow analysis* [28]. Specifically, the derived time scales reveal that the parameter g_{Ca} is inversely proportional to the time scales of the fastest and slowest variables. Hence, large g_{Ca} causes an increase in the speed of both variables, which shifts the balance in the time scales in the model from 2-fast/1-slow to 1-fast/2-slow. Accordingly, we show that the periodic orbits observed at high values of g_{Ca} can also be studied by 1-fast/2-slow analysis. Furthermore, we are able to explain the mechanism of bursting oscillations of the reduced IHC model using 2-fast/1-slow analysis by changing one of the model parameters that only affects the time scale of the slowest variable, namely the fraction of free cytosolic calcium concentration, f_c. Finally, we demonstrate that by changing f_c, the slow variable (i.e. the intercellular Ca^{2+} concentration) becomes faster and the reduced IHC model exhibits *mixed mode oscillations (MMOs)* [28] that could be studied by applying 1-fast/2-slow analysis.

Discussion of the results along with conclusions are presented in Section 4.

2. Reduced IHC model

2.1. Derivation of the reduced IHC model

The original IHC model is defined by a set of four ordinary differential equations (ODEs) in [16] as follows:

$$\begin{aligned}
C_{\mathrm{m}}\frac{\mathrm{d}V_{\mathrm{m}}}{\mathrm{d}t} &= -I_{\mathrm{Ca}}(V_{\mathrm{m}},Ca) - I_{\mathrm{K}}(V_{\mathrm{m}},n,h) - I_{\mathrm{K_{Ca}}}(V_{\mathrm{m}},Ca) - I_{\mathrm{leak}}(V_{\mathrm{m}}),\\
\frac{\mathrm{d}n}{\mathrm{d}t} &= \frac{n_\infty(V_{\mathrm{m}})-n}{\tau_{\mathrm{n}}(V_{\mathrm{m}})},\\
\frac{\mathrm{d}Ca}{\mathrm{d}t} &= f_{\mathrm{c}}\left(-\alpha I_{\mathrm{Ca}}(V_{\mathrm{m}},Ca) - k_{\mathrm{PMCA}}\frac{Ca^2}{Ca^2+K_{\mathrm{p}}^2} - \hat{k}_{\mathrm{SERCA}}Ca + \hat{p}_{\mathrm{ER}}(Ca_{\mathrm{ER}}-Ca)\right),\\
\frac{\mathrm{d}h}{\mathrm{d}t} &= \frac{1}{\tau_{\mathrm{h}}}(h_\infty(V_{\mathrm{m}})-h),
\end{aligned} \tag{1}$$

where V_{m} denotes the membrane potential, n the activation and h the inactivation variable for the voltage-gated K^+ channel, $Ca=[Ca^{2+}]_i$ the intercellular Ca^{2+} concentration, and $\hat{k}_{\mathrm{SERCA}}=\frac{k_{\mathrm{SERCA}}}{f_{\mathrm{c}}}$ and $\hat{p}_{\mathrm{ER}}=\frac{p_{\mathrm{ER}}}{f_{\mathrm{c}}}$.

The IHC model introduced in (1) is biophysical and hence the variables representing the membrane potential (V_{m}) and the intercellular calcium (Ca) as well as all model parameters, have dimensions usually used in this type of models such as (mV) and (μM). Model parameter values along with their respective units are given in Table A.1 in Appendix A.1, except for the parameters that we vary, namely g_{Ca}, $g_{\mathrm{K_{Ca}}}$, p_{ER}, f_{c}, which we specified throughout the text. We next perform a non-dimensionalisation of the model, with the view of estimating the characteristic rate of change of each variable, and obtaining an approximate model, in which the rate of change of the slowest variable is set to 0 (see Appendix A.1). As a result we obtain a reduced three-dimensional model.

Non-dimensionalisation is a process which eliminates the physical units of the variables in the model [29]. There are several objectives in making biophysical models non-dimensional. Here, we first explore the possibility to reduce the IHC model by comparing the speed of the state variables. According to the typical time scales in (A.12) calculated in Appendix A.1, the state variables V_{m} and n are much faster than the variables Ca and h. In the limit of τ_{h} ($\tau_{\mathrm{h}}\to\infty$) in (), we have $\frac{\mathrm{d}h}{\mathrm{d}t}=0$. Therefore one strategy to achieve a model reduction is to set $h(t)$ constant for all t.

The dynamic value of the inactivation variable h varies between 0 and 1 as it represents the probability of the voltage-gated K^+ channel 'gate' being inactivated, which depends on the membrane potential V_{m}, and changes along periodic solutions in the model. As we have shown previously [16,17] the periodic orbits of the IHC model are diverse, taking the form of single spikes, pseudo-plateau bursting and mixed type (complex) solutions with different numbers of spikes. Hence, in order to estimate a constant value for the variable h, we considered a large range of the parameters g_{Ca}, $g_{\mathrm{K_{Ca}}}$ and p_{ER}, where the original IHC model exhibits various periodic solutions and applied bifurcation analysis. As a result we were able to compute the midrange values between the maxima and minima of various periodic orbits and to calculate *average values* for the variable h as follows, $(h_{\mathrm{Max}}+h_{\mathrm{Min}})/2$. We then take the average of all averages, which gives the value $h=0.5732$. The following three dimensional model, where $h=0.5732$ is kept constant, will henceforth be referred to as the *reduced IHC model*.

$$\begin{aligned}
C_{\mathrm{m}}\frac{\mathrm{d}V_{\mathrm{m}}}{\mathrm{d}t} &= -I_{\mathrm{Ca}}(V_{\mathrm{m}},Ca) - I_{\mathrm{K}}(V_{\mathrm{m}},n) - I_{\mathrm{K_{Ca}}}(V_{\mathrm{m}},Ca) - I_{\mathrm{leak}}(V_{\mathrm{m}}),\\
\frac{\mathrm{d}n}{\mathrm{d}t} &= \frac{n_\infty(V_{\mathrm{m}})-n}{\tau_{\mathrm{n}}(V_{\mathrm{m}})},\\
\frac{\mathrm{d}Ca}{\mathrm{d}t} &= f_{\mathrm{c}}\left(-\alpha I_{\mathrm{Ca}}(V_{\mathrm{m}},Ca) - k_{\mathrm{PMCA}}\frac{Ca^2}{Ca^2+K_{\mathrm{p}}^2} - \hat{k}_{\mathrm{SERCA}}Ca + \hat{p}_{\mathrm{ER}}(Ca_{\mathrm{ER}}-Ca)\right).
\end{aligned} \tag{2}$$

2.2. Mapping the behaviour of the reduced to the original IHC model

Before completing the derivation of the non-dimensional form of the reduced IHC model we verify below that this model supports the range of dynamic behaviour observed in the original 4-dimensional IHC model [16,17]. To this end, we extend the analysis presented in [16,17] by performing bifurcation analysis using g_{Ca} as main bifurcation parameter and mapping the behaviour of the reduced and original IHC models. The behaviour of the original 4-dimensional and reduced 3-dimensional IHC model solutions can be investigated by examining the two-parameter bifurcation diagrams presented in Fig. 1 where for the sake of a fair comparison we keep the ranges of the bifurcation parameter values the same in both cases. Using the same notions as in [17], where periodic solutions are classified according to their number of large and prolonged spikes with small plateau oscillations, we use the notation $a+b$ for a periodic solution with a large spikes followed by b small spikes. For example, $1+4$ implies a periodic solution with 1 large spike followed by a prolonged spike with 3 small plateau oscillations.

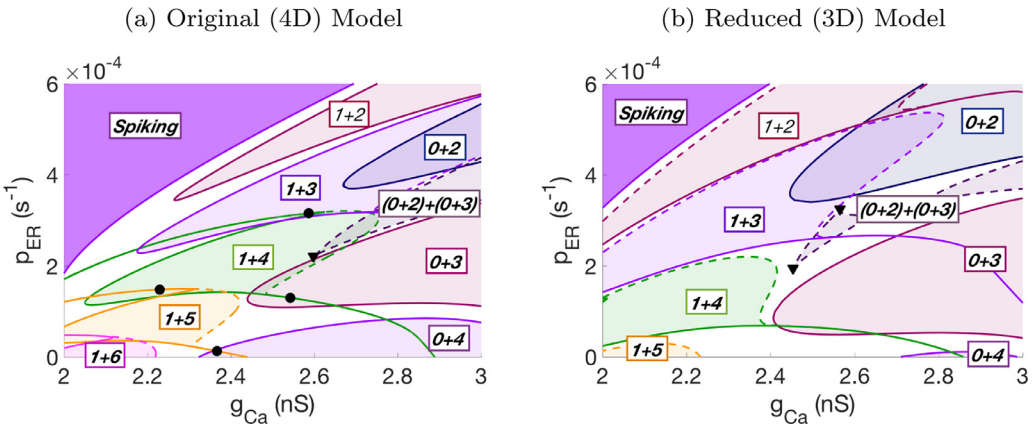

Fig. 1. Two-parameter bifurcation diagrams of the original and reduced IHC model when $g_{K_{Ca}} = 4$. Stable regions of solutions are delimited by tracing the period-doubling bifurcations (solid curves) and saddle-node bifurcation of periodic solutions (dashed curves), and are coloured accordingly. Black dots indicate possible *fold-flip bifurcation* [30] and filled triangles indicate *cusp* bifurcations. Note that we conventionally use the notation $a+b$ for periodic solution with a large spikes followed by b small spikes similar to Iosub et al. [17]. (For interpretation of the references to colour in this figure legend, the reader is referred to the web version of this article.)

In Fig. 1a, the stable regions of various periodic solutions, which are normal spiking, bursting (*0+N* and *(0+N)+(0+M)* solutions) and complex oscillations with one (normal) spike (*1+N* solutions) when $g_{K_{Ca}} = 4$, are coloured according to the total number of oscillations of the periodic orbits in the $g_{Ca} - p_{ER}$ plane. The stable regions of these periodic orbits are computed by tracing the bifurcations that result in a change of the stability of the periodic solutions, which are period-doubling (PD) and saddle-node bifurcation of periodic solutions (SNp). Additionally, the white regions also include chaotic (aperiodic) solutions of the model (as shown in Figure 3a in [15]). Fig. 1 reveals that the number of large (normal) spikes of complex periodic orbits decreases and, eventually, complex solutions become pseudo-plateau bursting solutions as g_{Ca} increases.

Next, using the same set of parameters, we also compute the stable regions of the periodic solutions of the reduced (3D) model in Fig. 1b. The two-parameter bifurcation diagrams depicted in Fig. 1 clearly demonstrate that the reduced IHC model can generate oscillatory behaviours consistent with the behaviour observed in the original IHC model. In this way we verify that the reduced (3D) IHC model approximates the dynamics found in the original (4D) IHC model reasonably well. We find that the PD and SNp curves that enclose the stable region of a periodic solution become very close to each other in the parameter space as shown in Fig. 1. At the values indicated by black dots, one of the multipliers of SNp curves crosses the unit circle at -1. Similarly, one of the multipliers of PD curves crosses the unit circle at +1, indicating the occurrence of a *fold-flip bifurcation* [30]. Note that the filled triangles show the other co-dimension two bifurcation points, which are the *cusp* bifurcation points where the two branches of SNp bifurcation curves of the *(0+2)+(0+3)* solutions meet tangentially [31].

2.3. Non-dimensional reduced IHC model

Having shown that the original and reduced IHC models support the variety of periodic solutions of interest we proceed by investigating the time scale separation in the reduced model and performing fast-slow analysis. The dimensionless form of the reduced IHC model could be written as:

$$\begin{aligned}\hat{\tau}_v \frac{dv}{d\tau} &= F(v,n,c)\\ \hat{\tau}_n \frac{dn}{d\tau} &= G(v,n)\\ \hat{\tau}_c \frac{dc}{d\tau} &= H(v,c)\end{aligned} \tag{3}$$

where the typical time scales are

$$\hat{\tau}_v := \frac{C_m}{Q_t g_{max}}, \quad \hat{\tau}_n := \frac{1}{\hat{\Gamma}_n Q_t}, \quad \hat{\tau}_c := \frac{Q_c}{Q_t f_c \alpha g_{Ca} Q_v} \tag{4}$$

and the functions $F(v, n, c)$, $G(v, n)$ and $H(v, c)$ on the right hand side of (3), and $g_{max} = \max(g_{Ca}, g_K, g_{K_{Ca}})$ along with the rest of the constants in (4) are given in Appendix A.1. It is important to note that the parameter g_{Ca} affects the time scales of both, v and c, in the case when g_{Ca} is the maximum conductance of the model as could be seen in (4). Additionally, the IHC model exhibits oscillatory behaviour when $0 < g_{Ca} < 60$ and $0 < g_{K_{Ca}} < 40$. Thus, considering the parameter values given

Table 1
Time scale constants for $g_{Ca} = 3$, $g_{Ca} = 4$, $g_{Ca} = 4.1$, $g_{Ca} = 22$ and $g_{Ca} = 24$ when the scaling parameter values are $Q_v = 100$ mV, $Q_c = 1$ μM, $Q_t = 1$ s.

	$g_{Ca} = 3$	$g_{Ca} = 4$	$g_{Ca} = 4.1$	$g_{Ca} = 22$	$g_{Ca} = 24$
$\hat{\tau}_v$	0.0024	0.0018	0.0017	0.0003	0.0003
$\hat{\tau}_n$	0.0051	0.0051	0.0051	0.0051	0.0051
$\hat{\tau}_c$	0.1137	0.0853	0.0832	0.0155	0.0142

in Table A.1 (Appendix A.1), $p_{ER} = 0.0015$, $f_c = 0.004$ and the scaling parameter values $Q_v = 100$ mV, $Q_c = 1$ μM, $Q_t = 1$s we obtain:

- $\hat{\tau}_v$ is typically an $O(10^{-3})$ or an $O(10^{-4})$;
- $\hat{\tau}_n$ is typically an $O(10^{-2})$;
- $\hat{\tau}_c$ takes a typical range of $[O(10^{-2}),\ O(10^{0})]$.

The above non-dimensionalisation suggests two scalings for the reduced model:

1-fast/2-slow scaling: this regime is obtained when $g_{max} \gg 1$ so that $\hat{\tau}_n, \hat{\tau}_c = O(10^{-2})$ (slow variables), while $\hat{\tau}_v = O(10^{-4})$ (fast variable). To interpret orbits in this regime we employ a *1-fast/2-slow analysis* [32];

2-fast/1-slow scaling: this regime is obtained when the parameters are fixed as in the 1-fast/2-slow scaling, with the exception of f_c, which affects solely $\hat{\tau}_c$ and which is fixed to a small value. In this setting it is possible to obtain a different separation of time scales, whereby $\hat{\tau}_c = O(10^{0})$ (slow variable), and $\hat{\tau}_v, \hat{\tau}_n = O(10^{-2})$ (fast variables). For this scaling we apply a *2-fast/1-slow analysis* [27].

We note that the parameter f_c, representing the fraction of free cytosolic calcium, directly affects only the time scale of c and could be taken small as it implicitly accounts for calcium buffering, which slows down the dynamics of calcium dramatically [33]. Appendix A.2 contains further details on the fast-slow model decomposition we have performed.

3. Fast-slow analysis of the reduced IHC model

3.1. Effects of varying g_{Ca} on the time scales

The typical time scales (4) reveal that the calcium conductance g_{Ca} affects the time scale constants of the intercellular calcium ($\hat{\tau}_c$) and the membrane voltage ($\hat{\tau}_v$) in the case when g_{Ca} is the maximum of the conductances. As mentioned above, g_{Ca} is inversely proportional to both $\hat{\tau}_v$ and $\hat{\tau}_c$. Thus, increasing g_{Ca} makes both the fast variable (v) and the slow variable (c) faster by decreasing their time scale constants.

In order to investigate the dependence of the model solutions on varying g_{Ca} we compute a one-parameter bifurcation diagram using g_{Ca} as a bifurcation parameter (Fig. 2, where $g_{K_{Ca}} = 2$, $p_{ER} = 0.0015$). For small values of the control parameter g_{Ca}, the stable equilibria (blue curve) undergo a supercritical Hopf bifurcation (HB_1) that gives rise to a family of stable limit cycles. The inset in Fig. 2 depicts the family of complex periodic orbits with 1 large spike and a burst made of 2 plateau oscillations (*1+2* solution). As g_{Ca} increases, the reduced IHC model exhibits single spike solutions that terminate at a homoclinic bifurcation HC*.

Table 1 summarises the typical time scale constants for the representative periodic orbits shown in Fig. 2, namely $g_{Ca} = 3$ for a small single limit cycle, $g_{Ca} = 4$ for the complex periodic orbit (*1+2* solution), $g_{Ca} = 4.1$ for a bursting solution with two small spikes, $g_{Ca} = 22$ for a large single limit cycle and $g_{Ca} = 24$ for a mixed mode oscillation (MMO). As seen in Table 1 for small values of g_{Ca} there are three clearly different and not very well separated time scales in the model. The result of applying 2-fast/1-slow and 1-fast/2-slow analyses (see Appendix A.2) for $g_{Ca} = 4$ and $g_{Ca} = 4.1$ is shown in Fig. 3, which depicts the fast subsystems (a) and (c) and critical manifolds (b) and (d) in the model. This figure demonstrates the challenges faced by the fast-slow analysis in these cases since the limit cycles of the full model do not closely follow neither the manifolds of fast nor slow subsystems. However, detailed inspection of the bifurcation diagrams shown in Fig. 3 indicates that the active phase of the bursting solutions could be somewhat explained by the fast subsystem (see Fig. 3(a) and (c)) while the silent phase appears to follow the critical manifold (see Fig. 3(b) and (d)).

Furthermore, as g_{Ca} increases, the level of intracellular calcium in the model increases significantly, i.e. $0 < c < 4$ (as shown in Fig. A.2(a) in Appendix A.1). Hence, a scaling parameter for calcium $Q_c = 4$ would be more appropriate in this case. Since the amplitude of voltage also increases, the time scale function for n increases and its maximum becomes $\hat{\tau}_n = 400$ (see Fig. A.3 in Appendix A.1). Also, the calcium current in the voltage equation (3) is no longer bounded by 1 when g_{Ca} is large. In order to keep it bounded by 1, we have to scale it by its maximum over a period of the limit cycle when $g_{Ca} = 24$, which is $\max(I_{Ca}) = 4$ (an illustration of the effects of these scalings is given in Fig. A.2(b) and (c) in Appendix A.1). Now, if we consider these rescaling constants the right hand sides in (3) become of the same order as shown in Fig. A.2(d) in Appendix A.1. This yields new typical time scales as follows, $\hat{\tau}_v = 0.0018$, $\hat{\tau}_n = 0.0025$ and $\hat{\tau}_c = 0.0568$. Comparing these time scale constants with those in Table 1, we could see that the fastest (v) and the slowest variables (c) become faster as

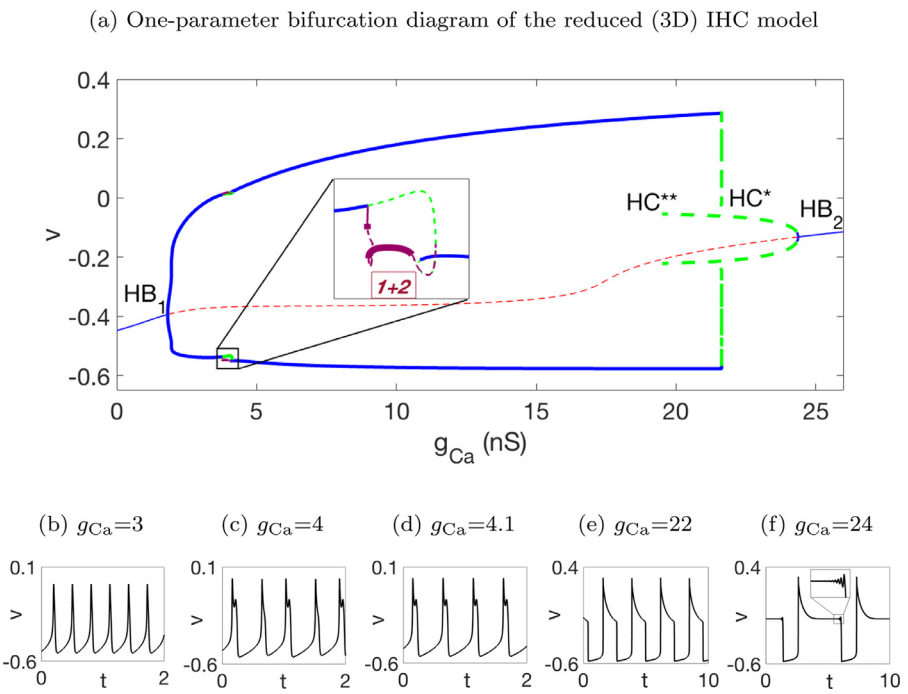

Fig. 2. (a) One-parameter bifurcation diagram of the reduced (3D) IHC model in the parameter g_{Ca} when $g_{K_{Ca}} = 2$, $p_{ER} = 0.0015$, $f_c = 0.004$, and all other parameters of the IHC model are given in Table A.1. The region of complex periodic orbit, $1+2$ solution, is magnified in the middle of the diagram. Solid thin blue lines represent stable equilibria and the dashed red line represents unstable equilibria. Solid thick blue lines represent stable limit cycles and the dashed green lines represent unstable limit cycles. HB: Hopf bifurcation, TR: Torus bifurcation, HC: Homoclinic bifurcation. We plot the time series solutions of some of the representative periodic orbits when (b) $g_{Ca} = 3$ (single spike), (c) $g_{Ca} = 4$ (complex: *1+2* solution), (d) $g_{Ca} = 4.1$ (bursting: *0+2* solution), (e) $g_{Ca} = 22$ (large periodic orbit) and (f) $g_{Ca} = 24$ (MMO) below the bifurcation diagram. (For interpretation of the references to colour in this figure legend, the reader is referred to the web version of this article.)

would be expected from the typical time scales in (3) since g_{Ca} is increased. These new time scales rather indicate two fast (v and n) and one slow (c) variable in the model, which we use next in order to investigating the model solutions for large g_{Ca}. In Fig. 4, we plot the fast subsystem bifurcation diagram of the model when $g_{Ca} = 24$ and superimpose the full system periodic orbit (black coloured) onto the fast subsystem diagram (see Appendix A.2). Clearly, the periodic orbit follows the stable equilibrium branches (solid blue curves) in Fig. 4a, projected onto two dimensions. Furthermore, the 2-fast/1-slow analysis indicates that the mechanism behind termination of the active phase (i.e. by which the trajectory of periodic orbit jumps from the upper equilibrium branch to the lower branch) could be via a slow passage through a Hopf bifurcation [34] as seen in Fig. 4b depicting the three-dimensional phase space of the model.

For completeness we also present the results from applying 1-fast/2-slow analysis where n and c are the slow variables and v is the only fast variable in the model. The structure of the equilibria of the desingularised system when $g_{Ca} = 22$ shown in Fig. 5(a) is the same as the desingularised system when $g_{Ca} = 24$. Both have a folded node on F^u, a folded focus on F^l and a saddle equilibria of the desingularised system on the repelling sheet of the critical manifold. However, the equilibrium of the full model when $g_{Ca} = 22$ is a saddle with eigenvalues are $\lambda_1 = 99.29$, $\lambda_2 = 46.28$ and $\lambda_3 = -12.14$, but the equilibrium of the full model when $g_{Ca} = 24$ is a saddle-focus with eigenvalues, $\lambda_{1,2} = 10.34 \pm 123.62i$ and $\lambda_3 = -5.31$. These saddle equilibria of the desingularised systems when $g_{Ca} = 22$ and $g_{Ca} = 24$ are shown as red squares in Fig. 5. This explains why decreasing g_{Ca} from 24 to 22 leads to disappearance of the small oscillations at the end of the active phase (as shown in Fig. 2).

Now, if we superimpose the periodic orbit when $g_{Ca} = 22$ on the critical manifold in Fig. 5b, we note that the orbit behaves similarly as the orbit when $g_{Ca} = 24$ (see Fig. 5c). Specifically, the orbit moves according to the slow flow (denoted by cyan coloured single arrows) on the lower attracting sheet of the critical manifold. As it gets closer to the lower fold (F^l) curve, the attraction becomes weaker and the trajectory jumps up to the upper attracting sheet. Once it reaches the upper sheet, it follows the weak stable manifold (green curve) of the folded node on F^u. The orbit continues following the weak stable manifold after the node until getting near the saddle equilibrium of the slow flow denoted by a red square, where this path on the repelling sheet is also part of the two-dimensional unstable manifold of the saddle of the full model. Once the orbit gets closer to the saddle equilibrium, it moves to the lower attracting sheet of the critical manifold and completes the cycle. In Fig. 5c, small oscillations are seen near the saddle on the repelling sheet of the manifold (S^r) since this is a saddle-focus equilibrium of the full model in this case. Accordingly, the small oscillations spiral away from the equilibrium

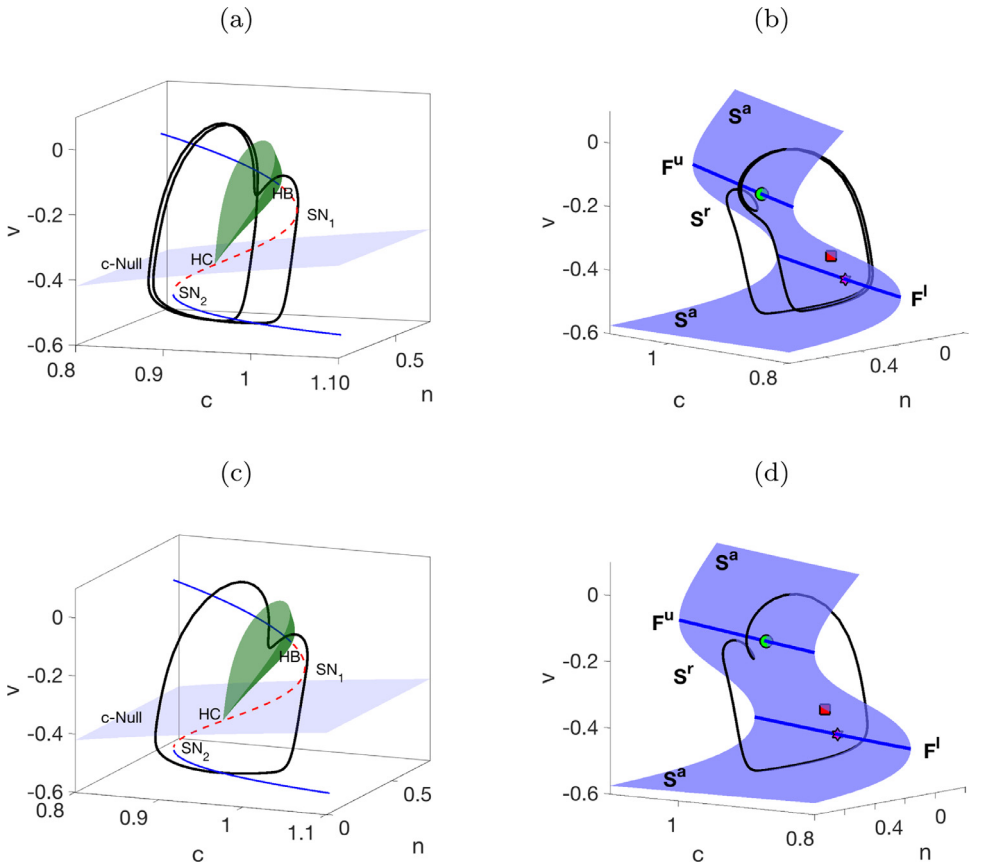

Fig. 3. Fast subsystem bifurcation diagrams and critical manifolds respectively when $g_{Ca} = 4$ (a)-(b) and $g_{Ca} = 4.1$ (c)-(d). For fast subsystem bifurcation diagrams in (a) and (c); the blue solid curves represent the stable equilibria and the red dashed curve represents unstable equilibria. The green surface represents the unstable periodic orbits. The transparent surface is the *c*-nullcline. HB: Hopf bifurcation, SN: Saddle-node bifurcation of equilibria, SNp: Saddle-node bifurcation of periodic orbits, HC: Homoclinic bifurcation. For the critical manifolds in (b) and (d); the green circle is a folded-node on the upper fold curve (F^u). The red square is the saddle equilibrium on the repelling sheet (S^r) at the critical manifold. The magenta star is a folded-node on the lower fold curve (F^l). (For interpretation of the references to colour in this figure legend, the reader is referred to the web version of this article.)

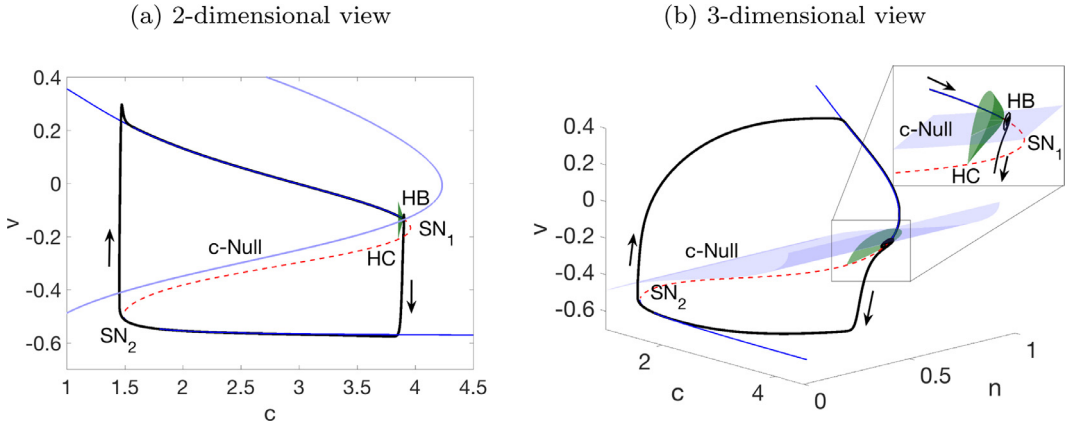

Fig. 4. Fast subsystem bifurcation diagram and 2-fast/1-slow analysis of the model when $g_{Ca} = 24$. Two dimensional (a) and three dimensional (b) views of the fast subsystem analysis of the model when $g_{Ca} = 24$. The blue solid curves represent the stable equilibria and the red dashed curve represents unstable equilibria. The green surface represents the unstable periodic orbits. The transparent surface is the c-nullcline. HB: Hopf bifurcation, SN: Saddle-node bifurcation of equilibria, HC: Homoclinic bifurcation. (For interpretation of the references to colour in this figure legend, the reader is referred to the web version of this article.)

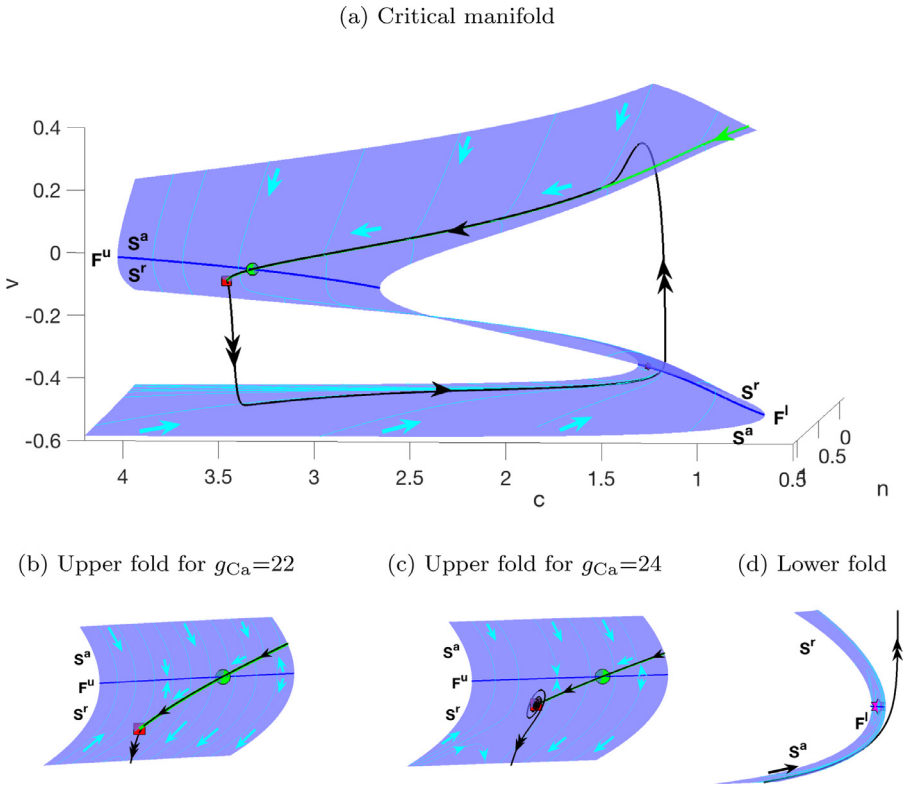

Fig. 5. (a) The periodic orbit (black coloured) when $g_{Ca} = 22$ (or $g_{Ca} = 24$) is superimposed on the critical manifold. (Note: Superimposing the periodic orbit (black coloured) when $g_{Ca} = 22$ and $g_{Ca} = 24$ on the critical manifold produces very similar views except around the upper folds, which we showed separately in (b) and (c).) The thin cyan curves are the trajectories of the slow flow. The green curve is the weak stable manifold of the folded-node (green circle) on the upper fold curve (F^u). (b) A magnification of the critical manifold around the upper fold when $g_{Ca} = 22$. The red square on the repelling sheet (S^r) is a saddle equilibrium. (c) A magnification of the critical manifold around the upper fold when $g_{Ca} = 24$. The red square on the repelling sheet (S^r) is a saddle-focus equilibrium. (d) A magnification of the critical manifold around the upper fold when $g_{Ca} = 22$ (or $g_{Ca} = 24$). The magenta star is a folded-node on the lower fold curve (F^l). (For interpretation of the references to colour in this figure legend, the reader is referred to the web version of this article.)

along its two dimensional unstable manifold [28]. As the oscillations grow and repeatedly intersect the repelling sheet, the trajectory of the orbit moves to the lower attracting sheet of the critical manifold and completes the cycle.

3.2. Effects of varying f_c on the time scales

In the previous section we investigate the effects of varying the parameter g_{Ca}. Although changes in g_{Ca} might be more realistic from application point of view as the expression (or number) of voltage gated Ca^{2+} channels could vary during development [24] for the sake of better mathematical tractability it is desirable to identify a parameter that controls the speed of only a single variable in the model. Indeed, as the typical time constants in (4) indicate the parameter f_c, representing the fraction of free to total cytosolic calcium concentration, makes a direct contribution to the time scale of the slow variable c without affecting the time scales of the variables v and n. Specifically, the slow time scale $\hat{\tau}_c = \frac{Q_c}{Q_t f_c \alpha g_{Ca} Q_v}$ is inversely proportional to the parameter f_c, and f_c does not appear in the fast time scale equations in (4). As f_c decreases, $\hat{\tau}_c$ increases, which implies that the slow variable c becomes slower. This allows us to investigate the dynamics of the various periodic solutions of the reduced IHC model by applying fast-slow analysis using a parameter that controls the rate of change of a single variable in the model.

In order to ensure that we capture as wide range of dynamic behaviours as possible we choose here a different set of parameters, namely $g_{Ca} = 2.4$, $g_{K_{Ca}} = 18$ and $p_{ER} = 0.00097$. This allows us to capture various type of solutions such as single spikes, bursting, complex oscillations with different number of large and small spikes and MMOs as the parameter f_c varies. We also note that the parameter $g_{K_{Ca}}$ is now the maximum conductance of the model.

Before turning our attention to analysing the reduced IHC model in the limit of $\epsilon = 0$, where ϵ represents the ratio between the fast and slow time scales (see Appendix A.2), it is instructive to look at the behaviour of the full model as f_c changes.

In Fig. 6, we plot representative time series solutions in the full model. As f_c increases, the model produces complex solutions with one large spike and different numbers of small spikes (from *1+11* to *1+4* solutions). Furthermore, the model

Table 2
Time scale constants for the values of f_c whose time series solutions are plotted in Fig. 6. The time scale constants for the variables v and c are $\hat{\tau}_v = 0.000394$ and $\hat{\tau}_n = 0.0051$, respectively.

f_c	0.000235	0.0004	0.0006	0.0010	0.00235	0.00244
$\hat{\tau}_c$	2.4184	1.4211	0.9474	0.5684	0.2419	0.2330

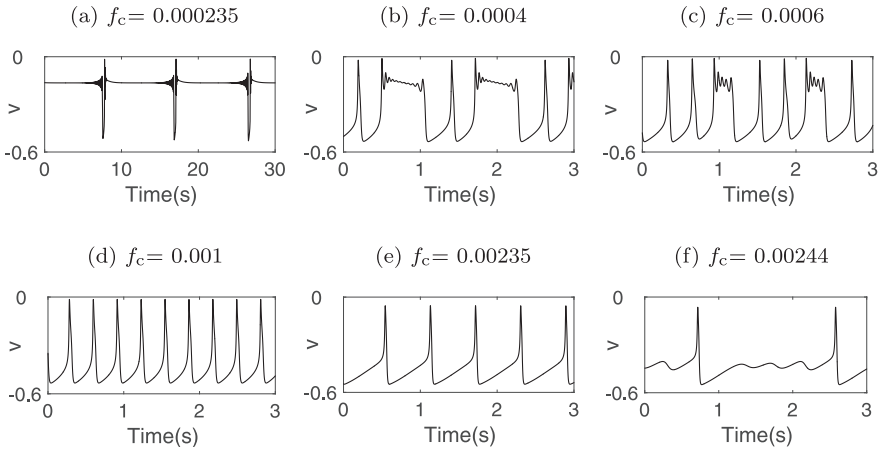

Fig. 6. Time series of periodic solutions as the parameter f_c varies and $g_{Ca} = 2.4$, $g_{K_{Ca}} = 18$, $p_{ER} = 0.00097$ are fixed. The model produces bursting solutions when $f_c = 0.000235$ (a), complex solutions with one large spike ($1+11$ solution) and with two large spikes ($2+5$ solution) when $f_c = 0.0004$ (b) and $f_c = 0.0006$ (c) respectively, single spike solutions when $f_c = 0.001$ (d) and $f_c = 0.00235$ (e), and mixed mode oscillations (MMOs) when $f_c = 0.00244$ (f). (For interpretation of the references to colour in this figure legend, the reader is referred to the web version of this article.)

also produces complex periodic orbits having two large spikes followed by a burst, for example *2+5, 2+4* and *2+3* solutions. We plot time series of complex periodic solutions *2+5* as a representative example (computed for $f_c = 0.0006$) in Fig. 6c. For a large range of the parameter f_c values, the model produces single spike solutions (for instance $f_c = 0.001$ and $f_c = 0.00235$ in Fig. 6d and e, respectively). We note that for $f_c = 0.00244$ (Fig. 6f, the periodic orbit is a combination of large and small sub-threshold oscillations (MMO) that are qualitatively different from the complex periodic orbits shown in Fig. 6a–c. In order to study further the periodic solutions described above we next apply slow-fast analysis (see Appendix A.2 for technical details).

3.2.1. Two fast-one slow analysis

Considering the scaling parameters $Q_v = 100$ mV, $Q_c = 1$ μM, $Q_t = 1s$ and using the parameter values given in Table A.1 in Appendix A.1, the time constants of the reduced IHC model for the periodic orbits shown in Fig. 6 are given in Table 2. Specifically, Table 2 indicates that the time constants for the Fig. 6a when $f_c = 0.000235$ are $\hat{\tau}_v = 0.000394$, $\hat{\tau}_n = 0.0051$ and $\hat{\tau}_c = 2.4184$ and the ratio between the fast and slow time scales $\epsilon = 0.000162$. In this case the variables v and n evolve on time scales that are much faster than the variable c. Therefore, for the given parameter values, we can define that v and n are the fast variables and c is the slow variable in the model. In Fig. 7, we plot two different views of the bifurcation diagram of the fast subsystem using c as a bifurcation parameter. As the bifurcation parameter c increases, the stable equilibrium branch (solid blue curve) of the fast subsystem undergoes a sub-critical Hopf bifurcation (HB_1) and loses stability (dashed red curve). This branch of equilibria regains stability at another sub-critical Hopf bifurcation (HB_2) obtained for larger values of c. A family of unstable limit cycles (green surface) emanates from (HB_1) and gains stability (blue surface) via a saddle-node bifurcation (SNp). This family of stable limit cycles vanishes in a homoclinic orbit (HC_1).

A periodic orbit computed for $f_c = 0.000235$ and shown in Fig. 6a, is superimposed on the fast subsystem bifurcation diagram in Fig. 7. Above the c-nullcline, which is indicated by c-Null, c increases since $\frac{dc}{d\tilde{\tau}} > 0$. Additionally, the amplitude of the small spikes within the bursting part of the periodic solution decreases until HB_1. This behaviour can be understood in terms of the type of the fast system equilibria, which are stable foci. As the trajectory of the full system moves away from HB_1 the amplitude of the small spikes within the burst starts to increase as the stability of the equilibria in the fast subsystem has changed and these are now unstable foci. However, since the c-nullcline is very close to the Hopf bifurcation HB_1, the slow passage through Hopf bifurcation [34] occurs in a very narrow range of c. As the amplitude of the small spikes increases the trajectory of the full system crosses the c-nullcline multiple times. The direction of the flow is reversed as the ratio between the average voltage above to below of the nullcline changes. Eventually the flow is attracted to the other stable regime of the fast subsystem, which is composed of stable limit cycles. Now c decreases ($\frac{dc}{d\tilde{\tau}} < 0$) while the trajectory follows the stable limit cycles region (blue surface). We note that the range of c is small in this case while the value of f_c is relatively large. This seems sufficient to force the trajectory to quickly leave the stable regime associated with

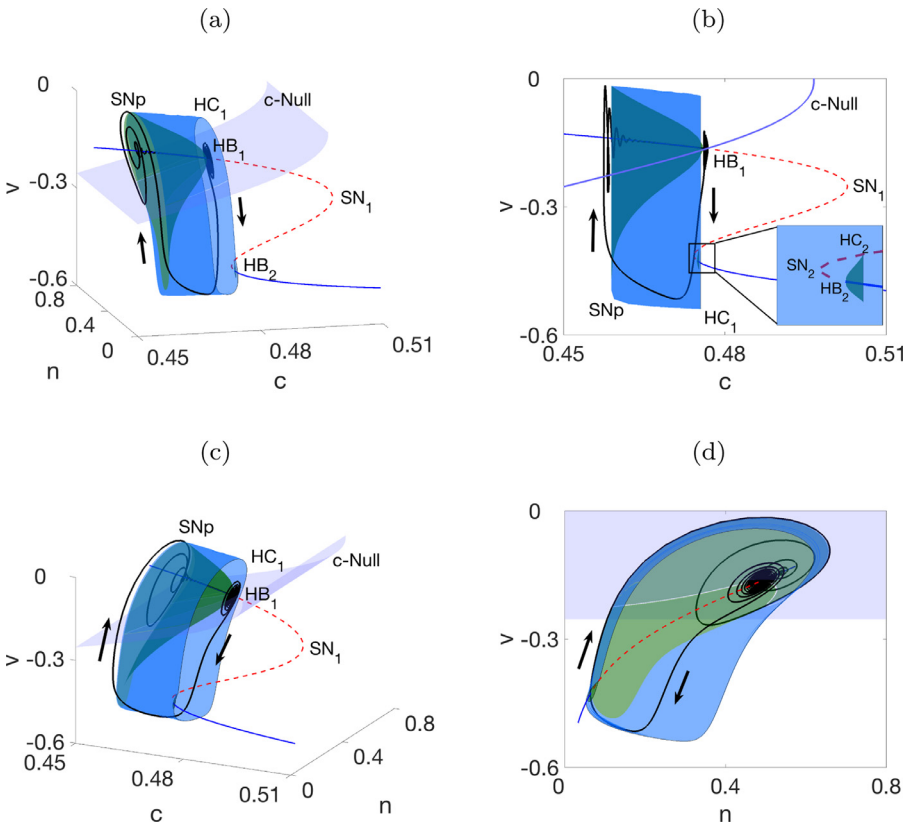

Fig. 7. Three dimensional and two-dimensional views of the fast subsystem for the periodic orbit when $f_c = 0.000235$. The bursting periodic orbit shown in Fig. 6a is superimposed on the figure. The blue solid curves represent the stable equilibria and the red dashed curve represents unstable equilibria. The blue and green surfaces represent the stable and unstable periodic orbits, respectively. The transparent surface is the c-nullcline. HB: Hopf bifurcation, SN: Saddle-node bifurcation of equilibria, SNp: Saddle-node bifurcation of periodic orbits, HC: Homoclinic bifurcation. (For interpretation of the references to colour in this figure legend, the reader is referred to the web version of this article.)

the limit cycles while moving left. As the trajectory crosses the saddle-node bifurcation of periodic orbits (SNp), it "rapidly" jumps to the upper stable equilibria branch.

In Fig. 8, we depict fast subsystem bifurcation diagrams for different values of f_c. As f_c increases, the reduced IHC model solutions do not follow the stable regions of the fast subsystem as closely as the bursting solution described above. This indicates that the 2-fast/1-slow analysis loses its explanatory power as expected for larger f_c values. This observation is consistent with the typical time scale constants' estimates presented in Table 2. In particular, depending upon the parameter values, the model could also be seen as having one fast and two slow variables. We investigate this in the following section.

3.2.2. One fast-two slow analysis

As f_c increases, the slow time scale $\hat{\tau}_c$ becomes smaller, therefore the slow variable c becomes faster. Thus, the model now could be regarded as having two slow variables (n and c) and one fast variable (v). Accordingly, we would like to interpret the behaviour of the full model periodic solution for $f_c = 0.00244$ in terms of the slow flow on the critical manifold (S-shaped blue surface) by superimposing the periodic orbit (black coloured) in Fig. 9. The manifold has two fold curves; at $v \approx -0.45$ (lower) and $v \approx -0.11$ (upper). The middle surface between fold curves is repelling S^r, and the top and bottom surfaces separated by the two fold curves of the manifold are attracting. The saddle-focus equilibrium [35], indicated by a red square in Fig. 9, has a pair of unstable complex conjugate eigenvalues ($\lambda_{1,2} = 1.21 \pm 16.65i$) and a real negative eigenvalue ($\lambda_3 = -6.56$). The interplay of the periodic orbit shown in Fig. 6f with the desingularised slow flow (see Appendix A.2) gives an insight into the overall structure of the full model solution. On the lower attracting sheet of the critical manifold S^a, the periodic orbit follows the strong stable manifold (green curve) of the folded node singularity on F^l. We colour code time when presenting the periodic orbit around the lower fold F^l (see the magnified region in Fig. 9). As time increases, which is indicated by the colour change from red to yellow on the periodic orbit, the small oscillations become larger around the saddle-focus equilibrium [35] on the repelling sheet, which repeatedly intersects the repelling and attracting sheets of the manifold. Then, it jumps to the upper attracting part of the critical manifold, where the attraction is not as strong as on the lower sheet. After the trajectory passes the upper fold, it jumps to the lower attraction sheet of the critical manifold and returns to the region near the singularity. Hence, it makes a full limit cycle and continues the periodic motion.

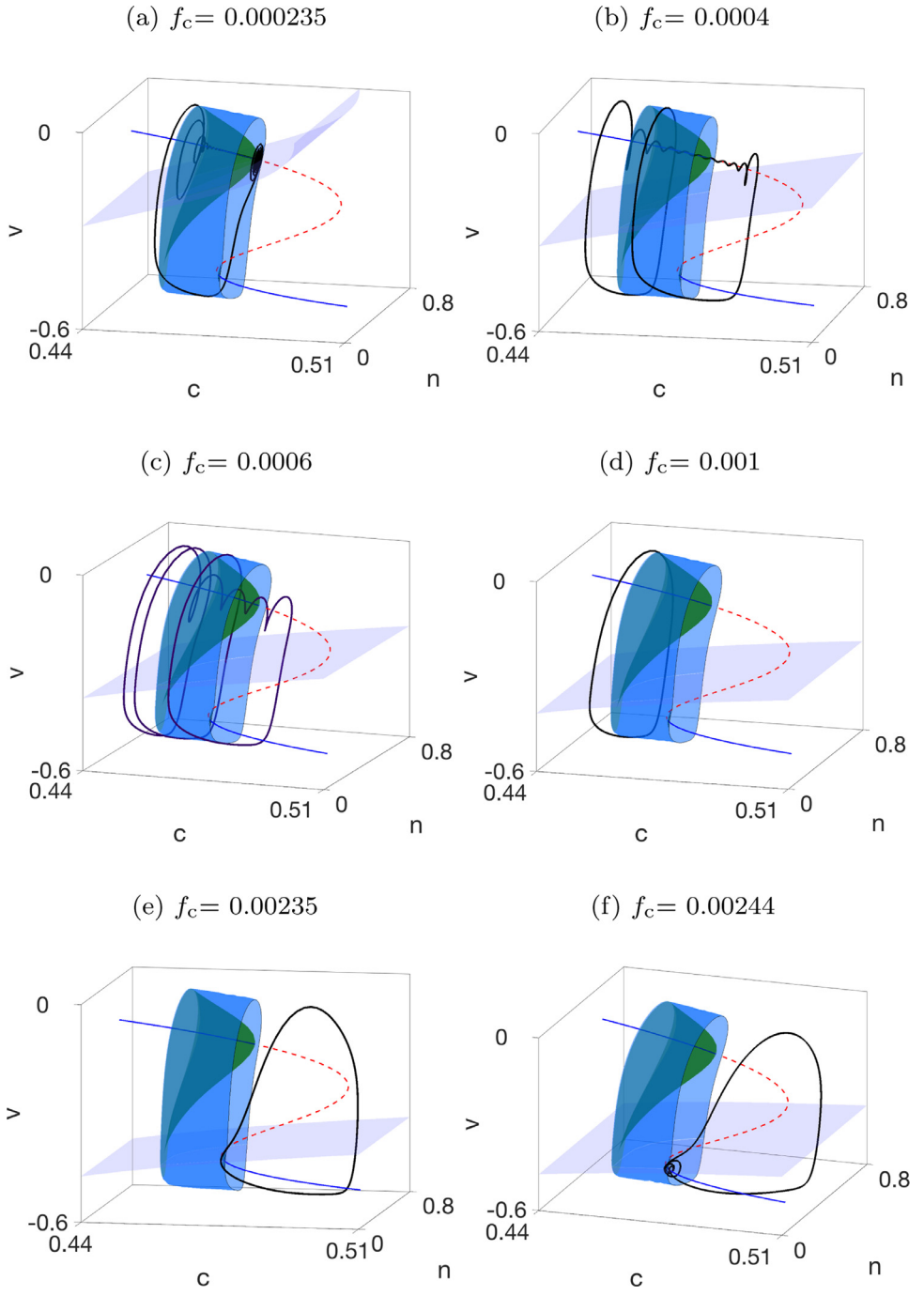

Fig. 8. Fast subsytem bifurcation diagrams and superimposed periodic orbits when (a) $f_c = 0.000235$ (Bursting), (b) $f_c = 0.0004$ (Complex: *1+11*), (c) $f_c = 0.0006$ (Complex: *2+5*), (d) $f_c = 0.001$ (Single spike), (e) $f_c = 0.00235$ (Single spike) and (f) $f_c = 0.00244$ (MMO). The blue solid and the red dashed curves represent the stable and unstable equilibria, respectively. The blue and green surfaces represent the stable and unstable periodic orbits, respectively. The transparent surface is the *c*-nullcline. (For interpretation of the references to colour in this figure legend, the reader is referred to the web version of this article.)

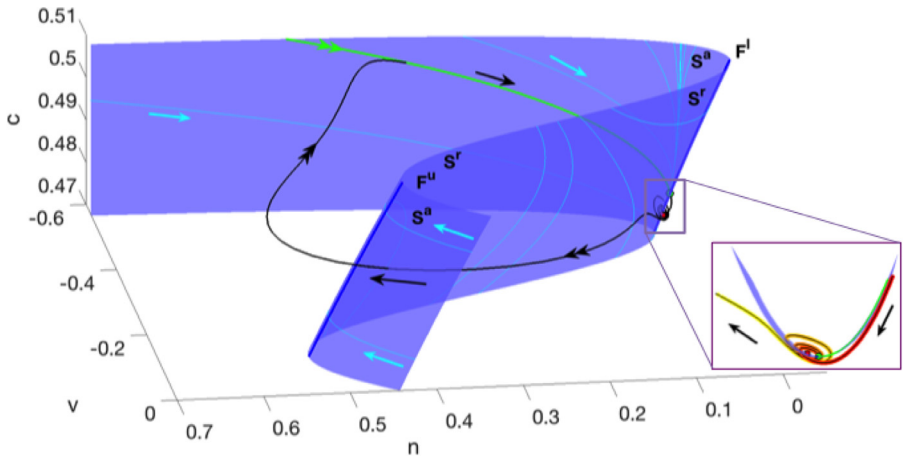

Fig. 9. The periodic orbit when $f_c = 0.00244$ is superimposed on the critical manifold. The green curve is the strong manifold of the node on the lower fold curve (F^l). The region of small oscillations around the saddle-focus equilibrium of the full model is magnified. The colour code on the orbit around the small oscillations represents the time along the periodic orbit i.e. time increases from red to yellow. (For interpretation of the references to colour in this figure legend, the reader is referred to the web version of this article.)

4. Discussion

In this paper we have made several contributions to better understanding of how immature IHC cell action potentials are shaped and regulated, and the mechanisms that underlie these dynamics. This is important as it could provide a greater insight into how such events may contribute to neuronal circuits and intrinsic development and more widely to understand how complex behaviours in other systems may be generated.

Firstly, we have investigated the role of varying a relevant biophysical parameter g_{Ca} (that has not been previously investigated) in controlling oscillatory model behaviour. As the value of g_{Ca} is proportional to the number of calcium channels in IHC that could vary during development of the nervous system [24] and are essential in IHCs [25] it is important to characterise the behaviour of the model in terms of this parameter. Specifically, we used g_{Ca} as a bifurcation parameter and showed that as this parameter increases, the complex oscillations lose their large spikes and become pseudo-plateau bursting solutions. This is observed over a large parameter range, resulting in a significant increase on the amplitude and duration of Ca^{2+} signals.

The second important contribution of this study is the reduction of the original (four-dimensional) IHC model [16] by non-dimensionalisation to a three-dimensional model that preserves the variety of model solutions corresponding to firing patterns observed in IHCs. We achieve this by identifying the slowest variable in the original model, i.e. the inactivation variable associated with the voltage-gated K^+ channels (h), and considering h as a fixed quantity resulting in a reduced (three-dimensional) IHC model. In order to verify that we do not lose the rich experimentally observed dynamics [17] of the original IHC model by fixing the slowest variable h, we carry out numerical continuation of a broad range of periodic attractors, such as normal spiking, pseudo-plateau bursting with several plateau oscillations and complex solutions with one and two large (normal) spikes, by tracing the bifurcations that result in a change of the stability of the periodic solutions (i.e. period-doubling (PD) and saddle-node bifurcation of periodic solutions (SNp)) in two parameters for both the original (4D) and the reduced (3D) IHC models. The two-parameter bifurcation diagrams confirm the qualitative agreement between the original and the reduced models. This allows us to investigate the simpler (3D) model in order to better understand its complex behaviour. This has the advantage that we no longer have to use projections of the original model in order to present the results of the analysis [36]. Specifically, we are able to capture the true representation of the trajectories in three dimensions and how various periodic orbits are organised without using phase-space projections.

Importantly non-dimensionalisation of the IHC model provides the typical time scale constants of the dynamic variables that enable us to classify the state variables as fast and slow according to the changes of the model parameters. Hence, having identified differences between the time scales of the reduced (3D) IHC model, we are able to apply fast-slow analysis in order to better understand the dynamic mechanisms underlying the behaviour of the model. The typical time scale constants reveal that the parameter g_{Ca} is inversely proportional to the time scales of both c and v when it dominates the other conductances in the model. We show that 2-fast/1-slow analysis could not fully explain the behaviour of the model solution for large g_{Ca} values. Applying 1-fast/2-slow analysis we are able to further demonstrate that the trajectory follows the unstable sheet of the critical manifold for a while until it reaches the saddle equilibrium of the slow flow, thus completing the analysis.

Furthermore, our analysis of the model bahaviour for larger g_{Ca} reveals mixed-model oscillations (MMOs) observed for values of g_{Ca} close to a torus bifurcation detected on the branch of small amplitude limit cycles originating from the rightmost Hopf bifurcation in Fig. 2. The small oscillations in these MMOs occur at the end of a depolarised plateau that could

be seen as an active phase of a bursting solutions. We show that such solutions are organised by a folded-node of the desingularised system and a saddle-focus equilibrium of the full model. We also show that although the dynamic structures of the desingularised system are the same for different values of g_{Ca}, the type of the full model equilibrium (i.e. focus or saddle-focus) can help in interpreting the overall behaviour of the various periodic orbits observed. In particular, the small oscillations of the MMOs when g_{Ca} is large could be explained by considering the saddle-focus equilibrium of the full model (Fig. 5).

The typical time scale constants also indicate that the parameter f_c (the fraction of free to total cytosolic calcium) appears only in the time scale of the variable c. Therefore, varying f_c affects solely the rate of change of c. We demonstrate that the reduced IHC model exhibits bursting solutions, complex solutions with one and two large spikes, normal spiking and MMOs as the parameter f_c increases, which makes the slow variable faster. The advantage of using f_c is that we are able to generate a broad range of periodic solutions by varying a single parameter f_c in the model. We showed that the mechanism underlying the bursting solutions can be understood by considering the fast subsystem dynamics i.e. the 2-fast/1-slow analysis when f_c is small. If we make the slow variable c faster by increasing the parameter f_c, the model exhibits MMOs, which we analyse applying 1-fast/2-slow analysis. It is important to note that the MMOs found by increasing f_c are different compared the MMOs found for large g_{Ca} and appear to be organised in a manner similar to the canonical model presented in [28].

Finally, we find that neither the 2-fast/1-slow nor the 1-fast/2-slow analysis can fully explain the mechanism of the complex solutions represented by mixture of action potentials/large spikes and bursting found in the model. We speculate that this might be due to the asymptotic nature of the typical time scale constants calculated by the non-dimensionalisation that are the lower bounds of the time scales of the state variables. However, time scale functions such as the time scale of n ($\tau_n(v)$) could exhibit rapid changes corresponding to large (action potential) spiking along a complex solution's trajectory as $\tau_n(v) = 0.0022 + 0.0029e^{-(vQ_v)/14.3}$. Such rapid changes might necessitate analysis of the model considering three-time scales [37]. Alternatively, different parts of complex solution's trajectory could be seen as governed by different subsystems and evolving under the fast, slow and super-slow flows [38]. Further research is needed in order to fully understand the dynamic mechanisms of such complex solutions given the time scales in the model.

Acknowledgement

KTA gratefully acknowledges the financial support of the EPSRC via grant EP/N014391/1.

Appendix A

A.1. Non-dimensionalisation of the IHC model

The IHC model is defined by a set of four ordinary differential equations (ODEs) in [16] as

$$\begin{aligned}
C_m \frac{dV_m}{dt} &= -I_{Ca}(V_m, Ca) - I_K(V_m, n, h) - I_{K_{Ca}}(V_m, Ca) - I_{leak}(V_m)\\
\frac{dn}{dt} &= \frac{n_\infty(V_m) - n}{\tau_n(V_m)}\\
\frac{dCa}{dt} &= f_c\left(-\alpha I_{Ca}(V_m) - k_{PMCA}\frac{Ca^2}{Ca^2 + K_p^2}\right) - k_{SERCA}Ca + p_{ER}(Ca_{ER} - Ca)\\
\frac{dh}{dt} &= \frac{1}{\tau_h}(h_\infty(V_m) - h)
\end{aligned} \tag{A.1}$$

where V_m denotes the membrane potential, (n) the activation and (h) the inactivation variable for the voltage-gated K^+ channel and $Ca = [Ca^{2+}]_i$ the intercellular Ca^{2+} concentration.

A.1.1. Dimensionless membrane voltage equation (v):

In order to eliminate the dimensions of the membrane voltage equation in (A.1), we have to rescale the state variables V_m and Ca as well as time t by some scaling constants that have the same dimensions with as variables V_m, Ca and t. Additionally, if we use the typical amplitude ranges for the state variables as these rescaling constants, the nondimensional state variables will vary between 0 and 1.

We have checked that the typical values of the membrane potential and the intercellular calcium of the IHC model are $V_m \in [-60, 0]$ mV and $Ca \in [0, 1]$ μM. Therefore, we consider the suitable choices for the membrane voltage and intercellular calcium as $Q_v = 100$ mV and $Q_c = 1$ μM, respectively.

Rescaling $V_m = vQ_v$, $Ca = cQ_c$ and $t = \tau Q_t$ with $Q_t = 1s$ eliminates the dimensions of V_m, Ca and t to get the new dimensionless variables v and c as well as time τ. Additionally, we also rescale the Nernst potentials V_{Ca}, V_K and V_{leak} by Q_v. Therefore, we obtain the dimensionless form of the membrane voltage (v) as

$$\frac{C_m}{Q_t g_{max}}\frac{dv}{d\tau} = -\hat{I}_{Ca}(v, c) - \hat{I}_K(v, n, h) - \hat{I}_{K_{Ca}}(v, c) - \hat{I}_{leak}(v) \tag{A.2}$$

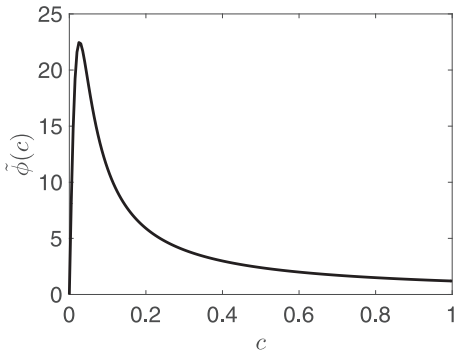

Fig. A.1. Evolution of the function $\tilde{\phi}(c)$ as c changes.

where $g_{max} = \max\{g_{Ca}, g_K, g_{K_{Ca}}, g_{leak}\}$ and the dimensionless currents $\hat{I}_X = \frac{I_X}{g_{max}Q_v}$ with X ∈ {Ca, K, K_{Ca}, leak}.

Scaling the conductances by g_{max} results in all terms on the right hand side (RHS) of the equation to be bounded (in absolute values) by one. Therefore, the typical time scale for the membrane voltage v is given by $\frac{C_m}{Q_t g_{max}}$.

A.1.2. Dimensionless calcium equation (c):

Let us recall the intercellular calcium equation of the reduced IHC model given in (A.1).

$$\frac{dCa}{dt} = f_c\Big(-\alpha I_{Ca}(V_m, Ca) - \phi(Ca)Ca - (\hat{k}_{SERCA} + \hat{p}_{ER})Ca + \hat{p}_{ER}Ca_{ER}\Big) \tag{A.3}$$

where $\hat{k}_{SERCA} = \frac{k_{SERCA}}{f_c}$, $\hat{p}_{ER} = \frac{p_{ER}}{f_c}$ and $\phi(Ca) = \frac{k_{PMCA}Ca}{Ca^2 + K_p^2}$.

Scaling $V_m = vQ_v$, $Ca = cQ_c$ and $t = \tau Q_t$, we get the dimensionless form of the calcium equation as

$$\frac{dc}{Q_t d\tau} = f_c\Big(-\xi \bar{I}_c(v, c) - \Phi\bar{\phi}(c)c - (\hat{k}_{SERCA} + \hat{p}_{ER})c + \hat{p}_{ER}c_{ER}\Big) \tag{A.4}$$

where $\xi = \frac{\alpha g_{Ca} Q_v}{Q_c}$, $\bar{I}_c(v, c) = \frac{I_{Ca}(V_m, Ca)}{g_{Ca}Q_v}$, $c_{ER} = \frac{Ca_{ER}}{Q_c}$, $\tilde{\phi}(c) = \phi(Ca)$, $\bar{\phi}(c) = \frac{\tilde{\phi}(c)}{\Phi}$ with $\Phi = \max_{0\le c\le 1}\tilde{\phi}(c)$, which is well defined since $\tilde{\phi}(c)$ is continuous (see Fig. A.1).

In order to make all terms on the RHS of the Eq. (A.4) bounded (in absolute values) by one, we estimate the values of constants on the RHS as

$$(\hat{k}_{SERCA} + \hat{p}_{ER}) \quad \text{is at most} \approx 10^3,$$
$$(\hat{p}_{ER}c_{ER}) \quad \text{is at most} \approx 10^3 \quad \text{and}$$
$$\xi = \frac{\alpha g_{Ca} Q_v}{Q_c} \quad \text{is at most} \approx 10^4$$

with the model parameters given in Table A.1 and considering the ranges of the bifurcation parameters p_{ER} and g_{Ca}. After rescaling the equation by ξ, all terms on the RHS are bounded (in absolute value) by one, and we obtain

$$\frac{Q_c}{Q_t f_c \alpha g_{Ca} Q_v}\frac{dc}{d\tau} = -\bar{I}_c(v, c) - \zeta_1\bar{\phi}(c)c - \zeta_2 c + \zeta_3 \tag{A.5}$$

where $\zeta_1 = \frac{\Phi Q_c}{\alpha g_{Ca} Q_v}$, $\zeta_2 = \frac{(\hat{k}_{SERCA} + \hat{p}_{ER})Q_c}{\alpha g_{Ca} Q_v}$ and $\zeta_3 = \frac{\hat{p}_{ER} c_{ER} Q_c}{\alpha g_{Ca} Q_v}$.

A.1.3. Dimensionless activation variable equation (n):

The equation of the activation variable (n) associated with the voltage-dependent potassium (K^+) channel is given by

$$\frac{dn}{Q_t d\tau} = \frac{1}{\tau_n(v)}(n_\infty(v) - n) \tag{A.6}$$

As we have seen, the variable n is already dimensionless. Since we would like to bound the RHS of the IHC model in (A.1) as a result of the process of non-dimensionalisation, we need only to check if the right hand side of (A.6) is bounded by one.

We have $0 \le n \le 1$ and $0 \le n_\infty(v) \le 1$, hence $|n - n_\infty(v)| \le 1$. Fig. A.3 shows the behaviour of the inverse of the voltage dependent time scale function of the gating variable, which is given by

$$\frac{1}{\tau_n(v)} = (0.0022 + 0.0029e^{-vQ_v/14.3})^{-1} \tag{A.7}$$

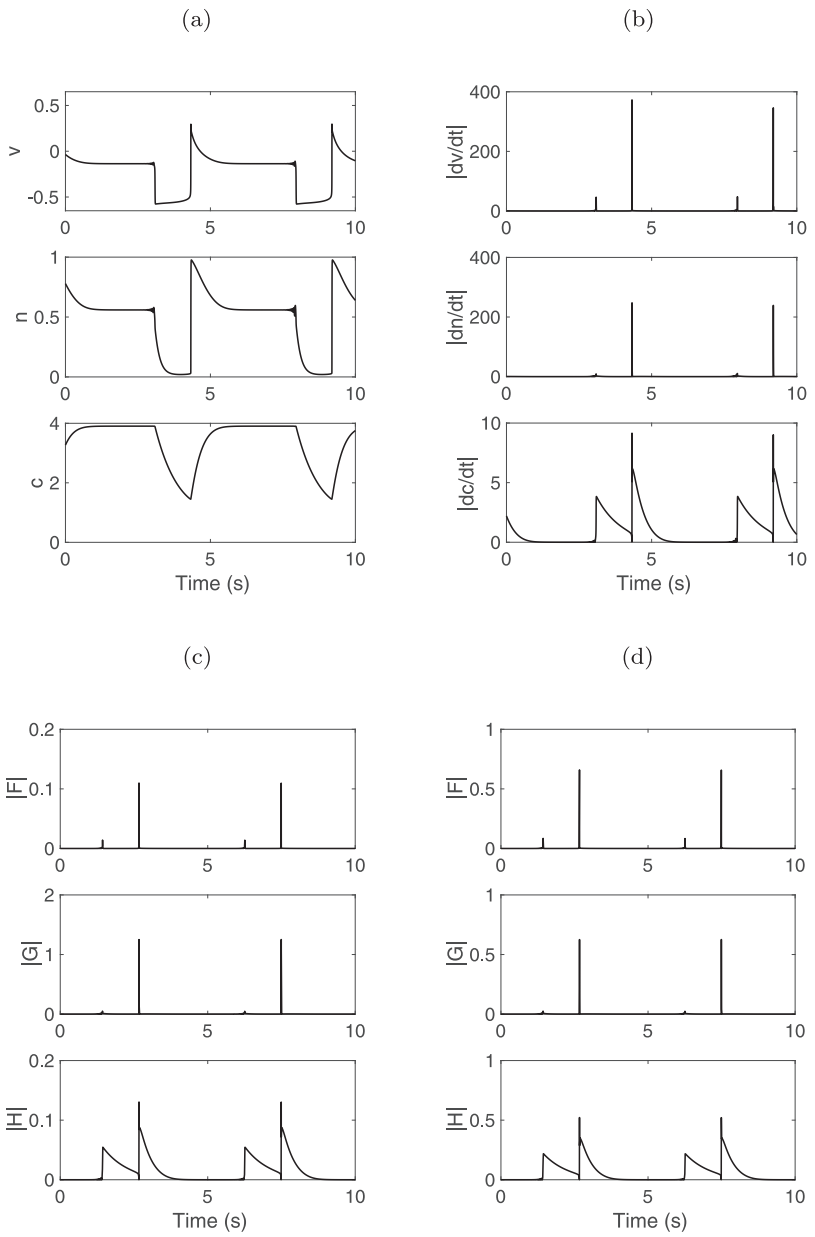

Fig. A.2. (a) Time series for the orbit shown in Fig. 4(a). (b) Right-hand side evaluated along the solution in (a), highlighting a difference in magnitudes of the respective components. (c) Right-hand side of (3) evaluated along the solution in (a). (d) A further rescaling with $Q_c = 4$, $\hat{\tau}_n = 400$, $\hat{\tau}_v = C_m/4$, leads to a right-hand side of order 1.

Let $\hat{\tau}_n := \max_{-0.6\leq v\leq 0} \frac{1}{\tau_n(v)}$. Therefore, we can rescale the function $\frac{1}{\tau_n(v)}$ by its maximum to get a new dimensionless time scale function, which is bounded (in absolute values) by one; i.e.

$$\frac{1}{\bar{\tau}_n(v)} := \frac{1/\tau_n(v)}{\hat{\tau}_n}$$

Hence, the equation of the activation variable n in (A.6) becomes

$$\frac{1}{\hat{\tau}_n Q_t}\frac{dn}{d\tau} = \frac{1}{\bar{\tau}_n(v)}(n_\infty(v) - n) \tag{A.8}$$

This scaling makes the RHS of the equation dimensionless and bounded (in absolute values) by one. Therefore, the typical time scale for the activation variable is given by $\frac{1}{\hat{\tau}_n Q_t}$.

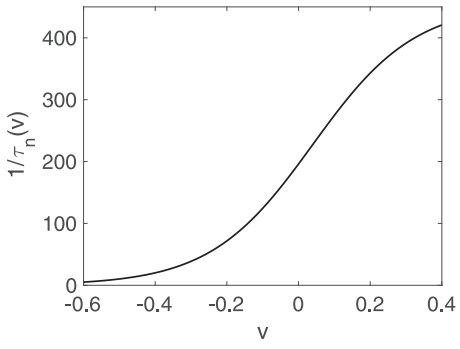

Fig. A.3. Evolution of the function $\frac{1}{\tau_n(v)}$ in (A.7) as v changes in its typical range.

A.1.4. Dimensionless inactivation variable equation (h):

The rate of change in the inactivation variable h is represented by

$$\frac{dh}{dt} = \frac{1}{\tau_h}(h_\infty(V_m) - h) \tag{A.9}$$

Similar to the activation variable (n), the inactivation variable (h) is already dimensionless, and moreover its time constant is already given in the model by τ_h, which is equal to 0.55. Therefore, the typical time scale for the inactivation variable is the constant of the time derivative of

$$\frac{\tau_h}{Q_t}\frac{dh}{d\tau} = h_\infty(v) - h \tag{A.10}$$

which is $\frac{\tau_h}{Q_t}$, which is equal to 0.55.

A.1.5. The dimensionless IHC model

Thus, the dimensionless form of the IHC model in (A.1) can be written as

$$\hat{\tau}_v\frac{dv}{d\tau} = F(v, n, c, h)$$
$$\hat{\tau}_n\frac{dn}{d\tau} = G(v, n)$$

Table A.1
Parameter values used in the IHC model .

Parameter	Value	Dimension	
Voltage-gated Ca^{2+}	V_{Ca}	−60	mV
current (I_{Ca})	V_{mL}	−26.7	mV
	s_m	11.5	mV
	K_q	0.6	µM
Ca^{2+}-activated K^+	V_K	60	mV
current ($I_{K_{Ca}}$)	k_s	1.25	µM
Voltage-gated K^+	g_K	2.85	nS
current (I_K)	V_K	60	mV
	V_n	−16	mV
	s_n	10	mV
	V_{h_1}	−60.5	mV
	s_{h_1}	6.8	mV
	V_{h_2}	−17.8	mV
	s_{h_2}	7.1	mV
	s_{τ_n}	14.3	mV
	τ_h	0.55	s
Leak current (I_{leak})	g_{leak}	0.12	nS
	V_{leak}	−20	mV
Intracellular Ca^{2+}	α	7.3	μ $MpA^{-1}s^{-1}$
Equation	k_{PMCA}	3.6	s^{-1}
	K_p	0.08	µM
	k_{SERCA}	1.2	s^{-1}
	c_{ER}	500	µM
Whole cell	C_m	0.0071	nF
parameters	d_{cell}	15	µM

$$\hat{\tau}_c \frac{\mathrm{d}c}{\mathrm{d}\tau} = H(v,c)$$
$$\hat{\tau}_h \frac{\mathrm{d}h}{\mathrm{d}\tau} = L(v,h) \tag{A.11}$$

where the typical time scales are

$$\hat{\tau}_v := \frac{C_\mathrm{m}}{Q_\mathrm{t} g_\mathrm{max}}, \quad \hat{\tau}_n := \frac{1}{\hat{I}_\mathrm{n} Q_\mathrm{t}}, \quad \hat{\tau}_c := \frac{Q_\mathrm{c}}{Q_\mathrm{t} f_\mathrm{c} \alpha g_\mathrm{Ca} Q_\mathrm{v}} \quad \text{and} \quad \hat{\tau}_h := \frac{\tau_\mathrm{h}}{Q_\mathrm{t}} \tag{A.12}$$

and the functions on the right hand sides are

$$F(v,n,h) = -\hat{I}_\mathrm{Ca}(v,c) - \hat{I}_\mathrm{K}(v,n,h) - \hat{I}_{\mathrm{K_{Ca}}}(v,c) - \hat{I}_\mathrm{leak}(v)$$
$$G(v,n) = \frac{1}{\hat{\tau}_\mathrm{n}(v)}(n_\infty(v) - n)$$
$$H(v,c) = -\bar{I}_\mathrm{c}(v,c) - \zeta_1 \bar{\phi}(c) c - \zeta_2 c + \zeta_3$$
$$L(v,h) = h_\infty(v) - h$$

All terms on the right hand side of (A.11) are of an order one. Therefore, the coefficients of the time derivatives of the nondimensional IHC model in (3) indicate the relative rates of evolution of the state variables.

We note that the parameter g_Ca affects both time scales of v and c when g_Ca is the maximum conductance of the model. Thus, considering the parameter values given in Table A.1, $p_\mathrm{ER} = 0.0015$, $f_\mathrm{c} = 0.004$ and the ranges for the conductances $0 < g_{Ca} < 60$ and $0 < g_{\mathrm{K_{Ca}}} < 40$ where the model exhibits oscillatory behaviour for the scaling parameter values $Q_\mathrm{v} = 100$ mV, $Q_\mathrm{c} = 1$ μM, $Q_\mathrm{t} = 1$s we get

- The typical time constant of v is of an order between $O(10^{-3})$ and $O(10^{-4})$;
- The typical time constant of n is of an order $O(10^{-2})$;
- The typical time constant of c takes a typical range of $[O(10^{-2}),\ O(10^{0})]$;
- The typical time constant of h is 0.55.

The typical time constants indicate that the state variables V_m and n are much faster than the variables Ca and h.

A.2. Slow/fast decomposition of the reduced IHC model

A.2.1. 2-fast/1-slow analysis

For some parameter values, we can define that v and n are the fast variables and c is the slow variable in the reduced IHC model. Thus, the ratio $\frac{\hat{\tau}_v}{\hat{\tau}_n}$ is of an order one and the ratio $\frac{\hat{\tau}_v}{\hat{\tau}_c}$ is very small.

Considering the nondimensional model in the fast time-scale, i.e. rescaling the system in (3) by replacing τ with $\tilde{\tau} = \frac{1}{\hat{\tau}_v}\tau$, we get

$$\frac{\mathrm{d}v}{\mathrm{d}\tilde{\tau}} = F(v,n,c)$$
$$\frac{\mathrm{d}n}{\mathrm{d}\tilde{\tau}} = G_1(v,n)$$
$$\frac{\mathrm{d}c}{\mathrm{d}\tilde{\tau}} = \epsilon H(v,c) \tag{A.13}$$

where

$$G_1(v,n) := \frac{\hat{\tau}_v}{\hat{\tau}_n} G(v,n) = \frac{\hat{I}_n C_\mathrm{m}}{g_\mathrm{max}} \left(\frac{n_\infty(v) - n}{\hat{\tau}_\mathrm{n}(v)} \right) \tag{A.14}$$

and the ratio between fast and slow time scales

$$\epsilon := \frac{\hat{\tau}_v}{\hat{\tau}_c} = \frac{C_\mathrm{m} f_\mathrm{c} \alpha g_\mathrm{Ca} Q_\mathrm{v}}{g_\mathrm{max} Q_\mathrm{c}}. \tag{A.15}$$

We consider the limit $\epsilon = 0$ in (A.13) to obtain the fast subsystem or layer equations [28,39] of the reduced IHC model for *2-fast/1-slow* case given by

$$\frac{\mathrm{d}v}{\mathrm{d}\tilde{\tau}} = F(v,n,c)$$
$$\frac{\mathrm{d}n}{\mathrm{d}\tilde{\tau}} = G_1(v,n)$$
$$\frac{\mathrm{d}c}{\mathrm{d}\tilde{\tau}} = 0 \tag{A.16}$$

Since $\frac{\mathrm{d}c}{\mathrm{d}\tilde{\tau}} = 0$, we can treat c as a parameter in the fast subsystem. Then, using the fast subsystem bifurcation structure, we will attempt to interpret the dynamics of the periodic solutions of the reduced IHC model.

A.2.2. 1-fast/2-slow analysis

On the other hand, for some other parameter values, the reduced IHC model could have only one fast variable v and two slow variables n and c. Thus, the ratio $\frac{\hat{\tau}_n}{\hat{\tau}_c}$ is of an order one and the ratio $\frac{\hat{\tau}_v}{\hat{\tau}_c}$ is very small.

So, if we re-cast the system (3) from τ to the slow time scale $\tilde{t} := \frac{1}{\hat{\tau}_c}\tau$, we obtain

$$\begin{aligned}\epsilon\frac{dv}{d\tilde{t}} &= F(v,n,c)\\ \frac{dn}{d\tilde{t}} &= G_2(v,n)\\ \frac{dc}{d\tilde{t}} &= H(v,c)\end{aligned} \tag{A.17}$$

where

$$G_2(v,n) := \frac{\hat{\tau}_c}{\hat{\tau}_n}G(v,n) = \frac{\hat{T}_n Q_c}{f_c \alpha g_{Ca} Q_v}\left(\frac{n_\infty(v)-n}{\hat{\tau}_n(v)}\right) \tag{A.18}$$

Writing the system (A.17) in the limit $\epsilon = 0$, we get

$$\begin{aligned}0 &= F(v,n,c)\\ \frac{dn}{d\tilde{t}} &= G_2(v,n)\\ \frac{dc}{d\tilde{t}} &= H(v,c)\end{aligned} \tag{A.19}$$

which is called the *slow subsystem* (or *reduced subsystem*) of the model [28,39]. We prefer to use the term "slow subsystem" instead of "reduced subsystem" in order to avoid confusion with the reduced IHC model.

The differential-algebraic system in (A.19) describes the *slow flow* that is restricted to the critical manifold [28,32,39], which is defined by

$$S := \{\,(v,n,c)\in\mathbb{R}^3 \quad | \quad F(v,n,c)=0\,\}. \tag{A.20}$$

where $F(v,n,c) := -\hat{I}_{Ca}(v,c) - \hat{I}_K(v,n) - \hat{I}_{K_{Ca}}(v,c) - \hat{I}_{leak}(v)$. The critical manifold has two fold curves (lower F^l and upper F^u) that separate the repelling and attracting sheets of the manifold (see Fig. 9).

In the equation $F(v,n,c)=0$, the variable n appears only in the voltage-dependent K^+ current that is given by $\hat{I}_K(v,n) = \frac{g_K}{g_{max}} n h(v-v_K)$. Therefore, $F(v,\,n,\,c)$ is linear in n, and so we can solve $F(v,n,c)=0$ for n in terms of v and c. Hence, we get

$$n := n(v,c) = \frac{-g_{Ca}m_\infty^2(v)q_\infty(c)(v-v_{Ca}) - g_{K_{Ca}}s_\infty(c)(v-v_K) - g_{leak}(v-v_{leak})}{g_K h(v-v_K)} \tag{A.21}$$

Taking the derivative of $F(v,n,c)=0$ with respect to time $\tilde{t}$ and applying the chain rule to $\frac{dF}{d\tilde{t}}=0$, we obtain

$$\begin{aligned}-\frac{\partial F}{\partial v}\frac{dv}{d\tilde{t}} &= \frac{\partial F}{\partial n}\frac{dn}{d\tilde{t}} + \frac{\partial F}{\partial c}\frac{dc}{d\tilde{t}}\\ -\frac{\partial F}{\partial v}\frac{dv}{d\tilde{t}} &= \frac{\partial F}{\partial n}G_2(v,n) + \frac{\partial F}{\partial c}H(v,c)\end{aligned}$$

This system is singular when $\frac{\partial F}{\partial v}=0$ i.e. at the fold curves. The flow is well defined on the critical manifold S, but not on the fold curves. In order to remove the singularities, we introduce a re-scaled time $\hat{t} := -\left(\frac{\partial F}{\partial v}\right)^{-1} d\tilde{t}$. Hence, we obtain the system

$$\begin{aligned}\frac{dv}{d\hat{t}} &= \frac{\partial F}{\partial n}G_2(v,n) + \frac{\partial F}{\partial c}H(v,c)\\ \frac{dc}{d\hat{t}} &= -\frac{\partial F}{\partial v}H(v,c)\end{aligned} \tag{A.22}$$

This system defines the *desingularised slow flow* [28,39]. A trajectory of the model near the singular limit passes through a folded singularity with finite speed unlike the other points on the fold curve, where trajectories have infinite speed [32].

References

[1] Marcotti W, Johnson SL, Holley MC, Kros C. Developmental changes in the expression of potassium currents of embryonic, neonatal and mature mouse inner hair cells. J Physiol 2003;548:383–400.
[2] Zachary S, Nowak N, Vyas P, Bonanni L, Fuchs PA. Voltage-gated calcium influx modifies cholinergic inhibition of inner hair cells in the immature rat cochlea. J Neurosci 2018;38(25):5677–87.
[3] Eckrich T, Blum K, Milenkovic I, Engel J. Fast Ca2+ transients of inner hair cells arise coupled and uncoupled to Ca2+ waves of inner supporting cells in the developing mouse cochlea. Front Mol Neurosci 2018;11.

[4] Kros CJ, Ruppersberg JP, Rüsch A. Expression of a potassium current in inner hair cells during development of hearing in mice. Nature 1998;394(6690):281.
[5] Marcotti W, Johnson SL, Rüsch A, Kros C. Sodium and calcium currents shape action potentials in immature mouse inner hair cells. J Physiol 2003;552:743–61.
[6] Beutner D, Moser T. The presynaptic function of mouse cochlear inner hair cells during development of hearing. J Neurosci 2001;21(13):4593–9.
[7] Johnson SL, Marcotti W, Kros CJ. Increase in efficiency and reduction in Ca2+ dependence of exocytosis during development of mouse inner hair cells. J Physiol 2005;563(1):177–91.
[8] Johnson SL, Eckrich T, Kuhn S, Zampini V, Franz C, Ranatunga KM, et al. Position-dependent patterning of spontaneous action potentials in immature cochlear inner hair cells. Nat Neurosci 2011;14(6):711.
[9] Hodgkin AL, Huxley AF. A quantitative description of membrane current and its application to conduction and excitation in nerve. J Physiol 1952;117(4):500–44.
[10] Chay TR, Keizer J. Minimal model for membrane oscillations in the pancreatic beta-cell.. Biophys J 1983;42(2):181–90.
[11] Stern JV, Osinga HM, LeBeau A, Sherman A. Resetting behavior in a model of bursting in secretory pituitary cells: distinguishing plateaus from pseudo-plateaus. Bull Math Biol 2008;70(1):68–88.
[12] Tsaneva-Atanasova K, Osinga HM, Rieβ T, Sherman A. Full system bifurcation analysis of endocrine bursting models. J Rheor Biol 2010;264(4):1133–46.
[13] Osinga H, Tsaneva-Atanasova K. Dynamics of plateau bursting depending on the location of its equilibrium. J Neuroendocrinol 2010;22(12):1301–14.
[14] Teka W, Tsaneva-Atanasova K, Bertram R, Tabak J. From plateau to pseudo-plateau bursting: making the transition. Bull Math Biol 2011;73(6):1292–311.
[15] Teka W, Tabak J, Vo T, Wechselberger M, Bertram R. The dynamics underlying pseudo-plateau bursting in a pituitary cell model. J Math Neurosci 2011;1(1):12.
[16] Szalai R, Tsaneva-Atanasova K, Homer ME, Champneys AR, Kennedy HJ, Cooper NP. Nonlinear models of development, amplification and compression in the mammalian cochlea. Philos Trans R Soc Lond A 2011;369(1954):4183–204.
[17] Iosub R, Avitabile D, Grant L, Tsaneva-Atanasova K, Kennedy HJ. Calcium-induced calcium release during action potential firing in developing inner hair cells. Biophys J 2015;108(5):1003–12.
[18] Clarke SG, Scarnati MS, Paradiso KG. Neurotransmitter release can be stabilized by a mechanism that prevents voltage changes near the end of action potentials from affecting calcium currents. J. Neurosci. 2016;36(45):11559–72.
[19] Johnson SL, Marcotti W. Biophysical properties of Cav1. 3 calcium channels in gerbil inner hair cells. J Physiol 2008;586(4):1029–42.
[20] Grant L, Fuchs P. Calcium- and calmodulin-dependent inactivation of calcium channels in inner hair cells of the rat cochlea. J. Neurophysiol. 2008;99(5):2183–93.
[21] Marcotti W, Johnson SL, Kros C. A transiently expressed SK current sustains and modulates action potential activity in immature mouse inner hair cells. J Physiol 2004;560:691–708.
[22] Zampini V, Johnson SL, Franz C, Lawrence ND, Münkner S, Engel J, et al. Elementary properties of Ca(v)1.3 Ca(2+) channels expressed in mouse cochlear inner hair cells. J Physiol 2010;588:187–99.
[23] Ferrario A, Merrison-Hort R, Soffe SR, Li W-C, Borisyuk R. Bifurcations of limit cycles in a reduced model of the *xenopus* tadpole central pattern generator. J Math Neurosci 2018;8(1):10.
[24] Sanes DH, Reh TA, Harris WA. Development of the nervous system. Elsevier; 2005.
[25] Brandt A, Striessnig J, Moser T. Cav1. 3 channels are essential for development and presynaptic activity of cochlear inner hair cells. J. Neurosci. 2003;23(34):10832–40.
[26] Bertram R, Rubin JE. Multi-timescale systems and fast-slow analysis. Math Biosci 2017;287:105–21.
[27] Rinzel J. Bursting oscillations in an excitable membrane model. In: Ordinary and partial differential equations. Springer; 1985. p. 304–16.
[28] Desroches M, Guckenheimer J, Krauskopf B, Kuehn C, Osinga HM, Wechselberger M. Mixed-mode oscillations with multiple time scales. SIAM Rev 2012;54(2):211–88.
[29] Murray JD. Mathematical biology: I. An introduction (Pt. 1). Interdisciplinary applied mathematics, vol. 17. 3 ed. Springer; 2002.
[30] Kuznetsov YA, Meijer HG, van Veen L. The fold-flip bifurcation. Int J Bifur Chaos 2004;14(07):2253–82.
[31] Kuznetsov Y. Elements of applied bifurcation theory. Applied mathematical sciences. Springer New York; 2004. ISBN 9780387219066.
[32] Bertram R, Tabak J, Teka W, Vo T, Wechselberger M, Kirk V, et al. Mathematical analysis of complex cellular activity. Springer; 2015.
[33] Keener J, Sneyd J. Mathematical physiology: I: cellular physiology. Interdisciplinary applied mathematics. Springer; 2009.
[34] Baer SM, Erneux T, Rinzel J. The slow passage through a Hopf bifurcation: delay, memory effects, and resonance. SIAM J Appl Math 1989;49(1):55–71.
[35] Izhikevich EM. Dynamical systems in neuroscience. MIT Press; 2007.
[36] Wegenkittl R, Loffelmann H, Groller E. Visualizing the behaviour of higher dimensional dynamical systems. In: Visualization'97., Proceedings. IEEE; 1997. p. 119–25.
[37] Nan P, Wang Y, Kirk V, Rubin JE. Understanding and distinguishing three-time-scale oscillations: case study in a coupled Morris–Lecar system. SIAM J Appl Dyn Syst 2015;14(3):1518–57.
[38] Vo T, Bertram R, Wechselberger M. Multiple geometric viewpoints of mixed mode dynamics associated with pseudo-plateau bursting. SIAM J Appl Dyn Syst 2013;12(2):789–830.
[39] Kuehn C. Multiple time scale dynamics. Applied mathematical sciences. Springer International Publishing; 2015. ISBN 9783319123165.